Nanocrystalline Mesoporous Tin Dioxide Prepared by the Sol−Gel Route from a Dialkoxydi(β-Diketonato)tin Complex

Thierry Toupance,* Odile Babot, Bernard Jousseaume, and Gil Vilaça

Laboratoire de Chimie Organique et Organométallique, UMR 5802 CNRS, Université Bordeaux 1, 351 Cours de la Libération, F33405 Talence Cedex, France

Received June 5, 2003. Revised Manuscript Received September 16, 2003

Nanocrystalline mesoporous tin dioxide materials have been obtained through the controlled hydrolysis of bis(2-methylbutan-2-oxy)di(pentan-2,4-dionato)tin followed by a thermal treatment at 400−550 °C. These materials have been carefully characterized by elemental analysis, FTIR, TGA-MS, XRD, MET, N_2 adsorption, and thermoporometry. They are composed of a porous network of aggregated nanoparticles with a mesoporosity arising from the interparticle space. A careful tuning of both hydrolysis ratio and calcination temperature allowed the preparation of powders with Brunauer−Emmett−Teller surface areas ranging from 50 to 150 $m^2 \cdot g^{-1}$, an average pore size between 45 and 100 Å, and a mean particle size ranging from 60 to 180 Å. The higher hydrolysis ratio favored the formation of mesoporous solids with high surface areas and low mean pore size diameter. The powders prepared at 550 °C might be advantageously used as semiconducting oxide materials in dye-sensitized photovoltaic devices.

Introduction

Stoichiometric tin dioxide is an n-type wide band gap ($E_g \approx 3.7$ eV) semiconductor showing high chemical and mechanical stabilities. Doped with fluorine or antimony, it exhibits high electronic conductivity and excellent IR reflectivity, with optical transparency in the visible range which remains almost unaffected. Tin dioxide-based materials therefore find widespread applications in various fields including catalysis,[1] photocatalysis,[2] solar energy conversion,[3] antistatic coatings,[4] electrochromic devices,[5] and transparent conductive electrodes.[6] More recently, its use as an anode material for lithium batteries has been developed,[7] with nanocrystalline[8] and/or F-doped tin dioxide powders[9] leading to larger reversible capacities than well-crystallized and undoped ones. However, the main application of these materials concerns gas sensing such as hydrogen,[10] carbon monoxide,[11] nitrogen oxides,[12] or volatile hydrocarbons (CH_4 or ethanol).[13] To a large extent, the sensor efficiency depends on the morphology and the thermal stability of the tin dioxide material used as active layer. Thus, on one hand the optimum crystallite size is known to be twice the depth of the space-charge layer (∼6 nm)[14] and, on the other hand, high specific areas are thought to improve both sensitivity and selectivity because the sensor response is related to the number of active sites chemically modified by the gas detected. In addition, a well-defined porosity would ensure a controlled diffusion of the gaseous species into the materials. Consequently, the development of synthetic procedures providing thermally stable mesoporous tin dioxide powders is a key-step toward the design of efficient gas sensors.

Many different methods have been proposed to obtain tin dioxide materials, including r.f. magnetron sputtering,[15] chemical vapor deposition,[16] spray-pyrolysis,[17]

* To whom correspondence should be addressed. E-mail: t.toupance@lcoo.u-bordeaux1.fr.

(1) Cebolla, V. C.; Bacaud, R.; Besson, M.; Cagniant, D.; Charcosset, H.; Oberson, M. *Bull. Soc. Chim. Fr.* **1978**, 935.

(2) (a) Miyauchi, M.; Nakajima, A.; Watanabe, T.; Hashimoto, K. *Chem. Mater.* **2002**, *14*, 2812. (b) Cun, W.; Jincai, Z.; Xinming W.; Bixian, M.; Guoying, S.; Ping'an, P.; Jiamo, F. *Appl. Catal. Part B. Environ.* **2002**, *39*, 269.

(3) (a) Bedja, T.; Hotchandani, S.; Kamat, P. V. *J. Phys. Chem.* **1994**, *98*, 4133. (b) Ferrere, S.; Zaban, A.; Gregg, B. A. *J. Phys. Chem. B* **1997**, *101*, 4490. (c) Srivastava, D. N.; Chappel, S.; Palchik, O.; Zaban, A.; Gedanken, A. *Langmuir* **2002**, *18*, 4160. (d) Kay, A.; Grätzel, M *Chem. Mater.* **2002**, 14, 2930. (e) Chappel, S.; Zaban, A. *Sol. Energy Mater. Sol. Cells* **2002**, *71*, 141.

(4) (a) Granqvist, C. G. *Solid State Mater. Sci.* **1990**, *16*, 291. (b) Robert, J. C. *U.S. Patent* 5494652, 1996.

(5) Olivi, P.; Pereira, E. C.; Longo, E.; Varella, J. A.; Bulhoes, L. O. *J. Electrochem. Soc.* **1993**, *140*, L81.

(6) (a) Chopra, K. L.; Major, S.; Pandya, D. K. *Thin Solid Films* **1983**, *102*, 1. (b) Goebbert, C.; Aegerter, M. A.; Burgard, D.; Nass, R.; Schmidt, H. *J. Mater. Chem.* **1999**, *9*, 253. (c) Cachet, H.; Gamard, A.; Campet, G.; Jousseaume, B.; Toupance, T. *Thin Solid Films* **2001**, *388*, 41.

(7) (a) Itoda, Y.; Kubota, T.; Matsufuji, A.; Maekawa, Y.; Miyasaka, T. *Science* **1997**, *276*, 1395. (b) Courtney, I. A.; Dahn, J. R. *J. Electrochem. Soc.* **1997**, *144*, 2045. (c) Retoux, R.; Brousse, T.; Schleich, D. M. *J. Electrochem. Soc.* **1999**, *146*, 2472.

(8) Zhu, J.; Lu, Z.; Aruna, S. T.; Aurbach, D.; Gedanken, A. *Chem. Mater.* **2000**, *12*, 2557.

(9) Kwon, C. W.; Campet, G.; Portier, J.; Poquet, A.; Fournès, L.; Labrugère, C.; Jousseaume, B.; Toupance, T.; Choy, J. H.; Subramanian, M. A. *Inter. J. Inorg. Mater.* **2001**, *3*, 211.

(10) Ansari, S. G.; Boroojerdian, P.; Sainkar, S. R.; Karekar, R. N.; Aiyer, R. C.; Kulkarni, S. K. *Thin Solid Films* **1997**, *295*, 271.

(11) Harrison, P. G.; Willett, M. J. *Nature* **1988**, *332*, 337.

(12) (a) Leblanc, E.; Jokela, K.; Perier-Camby, L.; Thomas, G. *J. Chim. Phys.* **1999**, *96*, 759. (b) Leblanc, E.; Perier-Camby, L.; Thomas, G.; Gibert, R.; Primet, M.; Gelin, P. *Sens. Actuators, B* **2000**, *62*, 67.

(13) Sberveglieri, G. *Sens. Actuators, B* **1992**, *6*, 239.

(14) Xu, C.; Tamaki, J.; Miura, N.; Yamazoe, N. *Sens. Actuators, B* **1991**, *3*, 147.

(15) Czapla, A.; Kusior, E.; Bucko, M. *Thin Solid Films* **1989**, *182*, 15.

10.1021/cm0344459 CCC: $25.00
Published on Web 11/08/2003

pyrolysis or decomposition of organotins followed by oxidation,[18] solid-state reactions[19] and precipitation processes.[20] Most of these techniques provide microcrystalline tin dioxide with rather low surface areas.[20] Since the discovery of mesoporous silicates prepared in the presence of amphiphilic molecules acting as supramolecular "templates",[21] the synthesis of mesoporous metal oxides by using organic surfactants has been widely investigated.[22] However, only a few examples of mesoporous tin dioxide have been reported according to this route, and the structures obtained are unstable after removal of the surfactant and thermal treatment above 350 °C.[23] The more promising results, i.e., Brunauer−Emmett−Teller surface areas around 100−150 $m^2 \cdot g^{-1}$ after thermal treatment at 400−500 °C, have been reported for materials prepared using a neutral and cationic templating approach[24] or a sonochemical[3c] method.

The sol−gel route could also be an appropriate way toward high specific area nanoporous metal oxides. A prime impediment was achieving monitoring of the competing hydrolysis and condensation reactions because precursors as metal alkoxides give ill-defined precipitates. For instance, hydrolysis of tetraalcoxytins leads to ill-defined materials exhibiting very low specific areas ($S_{BET} < 5$ $m^2 \cdot g^{-1}$) regardless of the solvent used. This was carried through the use of weakly hydrolyzable complexing agents, such as β-diketones[25] or carboxylic acids,[26] which diminished the hydrolysis−condensation rates by lowering the functionality of the sol−gel precursor and by poisoning the surface of the growing particles. Such an approach has been successfully exploited to prepare well-defined titanium[27] or tin dioxide[28] nanoparticles or amorphous tin dioxide xerogels.[29] However, no study has addressed the full morphological characterization of these SnO_2-based materials after thermal treatment and the complete elimination of the organics.

Scheme 1. Schematic Representation of Bis(2-methylbutan-2-oxy)Di(pentan-2,4-dionato)Tin 1

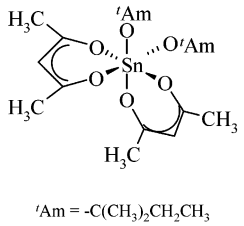

1

^{t}Am = -C(CH$_3$)$_2$CH$_2$CH$_3$

We have recently shown that nanocrystalline undoped or F-doped tin dioxide materials could be prepared by the sol−gel process from molecular precursors such as dialkoxy- or alkoxyfluorodi(β-diketonato)tin complexes.[30] This paper deals with the control of both morphology and texture of the powders prepared from bis(2-methylbutan-2-oxy)di(pentan-2,4-dionato)tin **1** (Scheme 1) by tuning the hydrolysis ratio and the temperature of the thermal treatment employed to crystallize the materials. In particular, emphasis has been put on the study of the mesoporous texture of both dried and calcined materials which constitutes a prerequisite before using them in gas sensing or photoelectrochemical devices.

Experimental Section

Materials. All manipulations of air- and moisture-sensitive compounds were carried out using standard Schlenk techniques under an atmosphere of dinitrogen. Solvents used were refluxed over calcium hydride (acetonitrile) or sodium/benzophenone (pentane) and collected by distillation. Infrared red spectra (KBr pellets) were recorded in the absorption mode using a Perkin-Elmer FTIR spectrophotometer. Elemental analyses were performed at the Center of Chemical Analysis of the Centre National de la Recherche Scientifique (Vernaison, France). The water content was determined by the classical Karl-Fisher method using methanol as a solvent and short contact time to avoid titration of surface hydroxyl groups. Bis(2-methylbutan-2-oxy)di(pentan-2,4-dionato)tin **1** was synthesized according to a previously reported procedure.[30a]

Preparation of Xerogels. To a stirred solution of **1** in acetonitrile was added dropwise a mixture of water and acetonitrile at room temperature. The molar ratio between the solvent and **1** was maintained around 50:1 and the hydrolysis ratio was varied from 2 to 10. After the mixture was stirred for 15−30 min, sol−gel transition took place and the resulting gels were aged at ambient temperature for 2 days. The solvent and volatile compounds were removed under reduced pressure at 50 °C to yield white powders which were then washed with *n*-pentane (15 × 50 mL). Subsequently, drying under vacuum at 100 °C gave the xerogels. In the following, the samples are labeled G_h^T where *h* and *T* stand for the hydrolysis ratio and the temperature of the thermal treatment, respectively.

(G_4^{100}) **1**, 38.4 g, 78.1 mmol; H_2O, 5.6 g, 322 mmol; CH_3CN, 160 mL. After drying, 36.2 g of a white powder was recovered. Elemental analysis (wt%). Calculated for $Sn(OH)_{1.6}O_1(C_5H_7O_2)_{0.4} \cdot 0.6H_2O$: Sn, 55.9; O, 30.1; C, 11.3; H_2O, 5.1. Found: Sn, 54.6; O, 28.5; C, 10.9; H_2O, 4.7.

(G_{10}^{100}) **1**, 12.3 g, 25.1 mmol; H_2O, 4.5 g, 251 mmol; CH_3CN, 65 mL. After drying, 4 g of a white powder was isolated. Elemental analysis (wt%). Calculated for $Sn(OH)_{0.78}O_{1.5}$-

(16) Kim, H. K.; Park, C. G. *J. Electrochem. Soc.* **1991**, *138*, 2408.
(17) Park, S. H.; Son, Y. C.; Willis, W. S.; Suib, S. L.; Creasy, K. E. *Chem. Mater.* **1998**, *10*, 2389.
(18) (a) Tamai, T.; Ichinose, N.; Agari, Y. *Macromol. Rapid. Commun.* **1999**, *20*, 179. (b) Pereira, A. G.; Porto, A. O.; Silva, G. G.; de Lima, G. M.; Siebald, H. G. L.; Neto, J. L. *Phys. Chem. Chem. Phys.* **2002**, *4*, 4528.
(19) Li, F.; Yu, X.; Pan, H.; Wang, M.; Xin, X. *Solid State Sci.* **2000**, *2*, 767.
(20) (a) Song, K. C.; Kang, Y. *Mater. Lett.* **2000**, *42*, 283. (b) Sergent, N.; Gélin, P.; Périer-Camby, L.; Praliaud, H.; Thomas, G. *Sens. Actuators, B* **2002**, *84*, 176.
(21) (a) Kresge, C. T.; Leconowicz, M. E.; Roth, W. J.; Vartuli, J. C.; Beck, J. S. *Nature* **1992**, *359*, 710. (b) Beck, J. S.; Vartuli, J. C.; Roth, W. J.; Leonowicz, M. E.; Kresge, C. T.; Schmitt, K. D.; Chu, C. T−W.; Olson, D. H.; Sheppard, E. W.; McCullen, S. B.; Higgins, J. B.; Schlenker, J. L. *J. Am. Chem. Soc.* **1992**, *114*, 10834.
(22) See for instance (a) Yang, P.; Zhao, D.; Margolese, I.; Chmelka, B. F.; Stucky, G. D. *Chem. Mater.* **1999**, *11*, 2813. (b) Galarneau, A.; Cambon, H.; Di Renzo, F.; Fajula, F. *Langmuir* **2001**, *17*, 83128.
(23) (a) Abdel-Fattah, T. M.; Pinnavaia, T. J. *J. Chem. Soc., Chem. Commun.* **1996**, 665. (b) Severin, K. G.; Abdel-Fattah, T. M.; Pinnavaia, T. J. *J. Chem. Soc., Chem. Commun.* **1998**, 1471. (c) Ulagappan, N.; Rao, C. N. R. *J. Chem. Soc., Chem. Commun.* **1996**, 1685. (d) Qi, L.; Ma, J.; Cheng, M.; Zhao, Z. *Langmuir* **1998**, *14*, 4. 1685.
(24) Chen, F.; Liu, M. *J. Chem. Soc., Chem. Commun.* **1999**, 1829.
(25) Sanchez, C.; Livage, J.; Henry, M.; Babonneau, F. *J. Non-Cryst. Solids* **1988**, *100*, 65.
(26) Roger, C.; Hampden-Smith, M. J. *J. Mater. Chem.* **1992**, *2*, 1111.
(27) Scolan, E.; Sanchez, C. *Chem. Mater.* **1998**, *10*, 3217.
(28) (a) de Monredon, S.; Cellot, A.; Ribot, F.; Sanchez, C.; Armelao, L.; Gueneau, L.; Delattre, L. *J. Mater. Chem.* **2002**, *12*, 2396. (b) Broussous, L.; Santilli, C. V.; Pulcinelli, S. H.; Craievich, A. F. *J. Phys. Chem. B* **2002**, *106*, 2855.
(29) Armelao, L.; Ribot, F.; Sanchez, C. In *Better Ceramics Through Chemistry VII*, Coltrain, B., Sanchez, C., Schaefer, D. W., Wilkes, G. L., Eds.; Materials Research Society: Pittsburgh, PA, 1996; p 387.
(30) (a) Gamard, A.; Campet, G.; Jousseaume, B.; Toupance, T. *Inorg. Chem.* **1999**, *38*, 4671. (b) Gamard, A.; Babot, O.; Jousseaume, B.; Rascle, M.-C.; Toupance, T.; Campet, G. *Chem. Mater.* **2000**, *12*, 419. (c) Boutet, S.; Gamard, A.; Jousseaume, B.; Toupance, T.; Campet, G.; Cachet, H. *Main Group Met. Chem.* **2002**, *25*, 59.

$(C_5H_7O_2)_{0.22}\cdot 0.45H_2O$: Sn, 63.8; O, 27.3; C, 7.1; H_2O, 4.4. Found: Sn, 62.3; O, 26.1; C, 7.1; H_2O, 4.7.

Thermolyses were realized by treating xerogels in air for 30 min at a temperature between 400 and 550 °C. The chemical composition of the resulting powders was determined by elemental analysis (wt%). G_4^{450} (exptl): Sn, 72.7; O, 20.7; C, 0.4. G_4^{550} (exptl): Sn, 78.3; O, 21.5; C, 0.2. G_{10}^{450}: (exptl) Sn, 73.8; O, 19.7; C, 0.5. G_{10}^{550}: (exptl) Sn, 75.3; O, 20.5; C, 0.3

Sample Characterization. Thermal studies were performed on a Netzsch STA simultaneous analyzer by using alumina crucibles. Thermogravimetry (TG) and derivative thermogravimetry were recorded in the range 50−650 °C under an air or argon flow at a heating rate of 5 °C·min^{-1}. Mass analyses were carried out on a Thermostar Balzers Instruments quadrupole spectrometer. Crystallinity of the materials was evaluated by powder X-ray diffraction using a Philips θ-2θ PW1820 diffractometer. TEM micrographs were obtained using a JEOL-JEM 100 SX microscope. The samples were prepared by a pickup from a suspension of dried or calcined powder in acetone.

The texture of the dried and calcined samples was analyzed by nitrogen adsorption isotherm (77 K) measurements. Data collection was performed by the static volumetric method, using an ASAP2010 (Micromeritics) apparatus. Before each analysis, the powders were degassed at 100 °C by vacuum pumping for a time interval high enough to obtain a constant pressure (∼ 3 μmHg). In pertinent cases, the mesopore size distribution was evaluated by the Barrett, Joyner, Halenda (BJH) method applied to the desorption branch of the nitrogen adsorption isotherm.[31] The calculation was performed by the Micromeritics software package which uses the recurrent method and applies the Harkins and Jura equation for the multilayer thickness.

Thermoporometry was also used to assess the pore size. This is a method of textural characterization based on thermal analysis of the liquid−solid transformation of a pure capillary condensate inside a porous framework.[32] The pore radii which can be estimated by thermoporometry are within the range 10−150 Å. Owing to the hydrophilic character of the samples, water was chosen as the test liquid for the thermoporometry. Samples were immersed into water, in the pan of a differential scanning calorimeter. A Perkin-Elmer DSC7 apparatus was used in the − 60 to +5 °C temperature range to measure the enthalpy of freezing in the pores. A first solidification/melting run was performed before studying the solidification at a cooling rate of 1 °C·min^{-1} in order to avoid any supercooling phenomenon. According to the comprehensive thermodynamical analysis develop by Brun et al.,[33] the freezing temperature of the liquid (water) is related to the pore radius (R_p) and the corresponding heat measured (ΔH) as follows:

$$R_p = -\frac{647}{\Delta T} + 5.7\ (\text{Å})$$

$$\Delta H = 332 + 7.43\,\Delta T + 5.56\ 10^{-2}\,(\Delta T)^2\ (\text{J}\cdot\text{g}^{-1})$$

where $\Delta T = T - T_0$ is depression of the freezing temperature

The differential distribution of pore volumes can be then calculated from the following equation:[34]

$$\frac{d\text{V}}{d\text{Rp}} = k\cdot P\cdot \frac{(\Delta T)^2}{\Delta H}$$

where P and k are the heat flow and a constant only depending on the experimental parameters, respectively.

Results

Synthesis and Characterization of the Xerogels. As Sanchez et al. have shown that polar coordinating solvents favor the formation of high specific area materials,[29] xerogels were prepared by controlled hydrolysis of **1** in acetonitrile. The latter was preferred to formamide or *N*,*N*-dimethylformamide as they are known to remain trapped in xerogels[30b] which leads to low surface areas and large pore sizes.[35] The hydrolytic procedure used was similar to that previously reported for related materials with a longer reaction time and drying under vacuum.[30] Thus, for both hydrolysis ratios investigated, gels were obtained 15−20 min after addition of water, subsequent aging for 2 days at room temperature, and drying under vacuum at 100 °C for several hours yielding white powders.

FTIR spectra of samples G_4^{100} and G_{10}^{100} have been recorded.[36] For G_4,[100] above 2000 cm^{-1}, a very broad absorption due to OH stretching modes is observed along with weak CH_3 stretching features at 2900 cm^{-1}. Key features observed below 2000 cm^{-1} include a band at 1624 cm^{-1} (shoulder) due to water deformation mode, resonances characteristic of acetylacetonato ligands coordinated to tin at 1567 and 1540 cm^{-1} (ν_{sym}(C−O) + ν_{asym}(C−C)), 1424 and 1363 cm^{-1} ($\delta(CH_3)$), 1287 cm^{-1}, 1025 and 938 cm^{-1} ($\rho(CH_3)$), and wide bands at 669 and 560 cm^{-1} assigned to Sn−O−Sn[37] and Sn−O[38] (belonging to Sn−OH groups) stretching vibrations, respectively. No evidence for acetonitrile and alkoxy groups is detected in the 2300−2200 and 1200−1000 cm^{-1} regions. Nonetheless, the shoulder at 1705 cm^{-1} (ketone stretching range) denotes the presence of a small amount of free acetylacetone likely trapped in the xerogel. In comparison with G_4^{100}, a decline of the chelating ligand content and an increase of the Sn−O−Sn amount are pointed out by IR spectroscopy for G_{10}^{100} as attested by the strong decrease of the bands assigned to acetylacetonate vibrations and the concomitant increase of the band at 670 cm^{-1}. As expected, these data are consistent with the formation of more condensed species when the hydrolysis ratio h was raised. Furthermore, according to the elemental analysis data, the formulas $Sn(OH)_{0.78}O_{1.5}(C_5H_7O_2)_{0.22}\cdot 0.45H_2O$ and $Sn(OH)_{1.6}O_1(C_5H_7O_2)_{0.4}\cdot 0.6H_2O$ may be proposed for G_{10}^{100} and G_4^{100}, respectively. This is in rather good accordance with the TG results.[36] Indeed, TG-DTG of G_{10}^{100} carried out in air exhibits three main mass losses of 5.4 (from 80 to 150 °C), 3.4 (from 150 to 280 °C), and 8.1% ((from 280 to 550 °C) to give a final residue of 82.8, close to the one expected (81.1%). Similarly, TG-DTG of G_4^{100} carried out in air exhibited three main mass losses of 3.8% (from 80 to 150 °C), 8.9% (from 150 to 280 °C), and 12.5% (from 280 to 550 °C) to give a final residue of 73.7%, close to that expected at 73%. The nature of the remaining organics in the xerogels was confirmed

(31) Barrett, E. P.; Joyner, L.; Halenda, P. P. *J. Am. Chem. Soc.* **1951**, *73*, 373.
(32) Brun, M.; Lallemand, A.; Quinson, J.-F.; Eyraud, C. *Thermochim. Acta* **1977**, *21*, 59.
(33) Quinson, J.-F.; Brun, M. In *Characterization of Porous Solids*; Unger, K. K., Ed.; Elsevier Science Publishers: Amsterdam, 1988; p 307.
(34) Gomez, F.; Denoyel, R.; Rouquerol, J. *Langmuir* **2000**, *16*, 4376.
(35) Boonstra, A. H.; Bernards, T. N. M.; Smits, J. J. T. *J. Non-Cryst. Solids* **1989**, *109*, 141.
(36) See Supporting Information.
(37) Kriegsman, H.; Hoffmann, H. M.; Geissler, H. *Z. Anal. Allg. Chem.* **1965**, *24*, 341.
(38) Morrison, J. S.; Haendler, H. M. *J. Inorg. Nucl. Chem.* **1967**, *29*, 393.

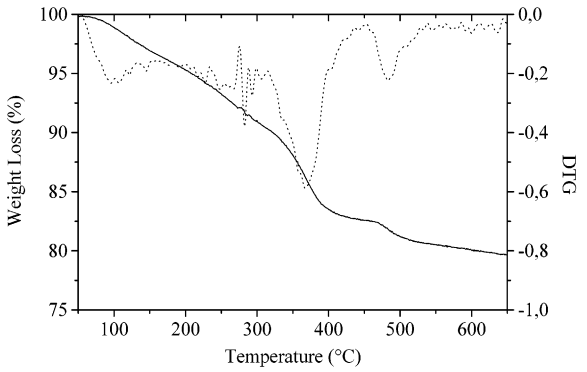

Figure 1. TG and DTG plots of xerogel G_{10}^{100} between 50 and 650 °C recorded under argon at 5 °C·min^{-1}.

by TGA-MS performed under an argon flow. For both samples studied, the shapes of the TG-DTG curves and the species evolved during the pyrolysis are similar. For instance, four mass losses are observed on TG traces of G_{10}^{100} (Figure 1) and the main molecules detected by MS measurements are H_2O, carbon dioxide, acetone, acetic acid, and acetylacetone traces.[36] The different pyrolysis stages can be rationalized as follows: (1) removal of adsorbed water (from 80 to 150 °C, 5% mass loss); (2) first step of pentan-2,4-dione decomposition with acetone release (from 150 to 300 °C, 5.1% mass loss); (3) loss of structural water, second step of pentan-2,4-dione degradation with acetone, acetic acid and carbon dioxide emissions (from 300 to 420 °C, 7.3% mass loss); and elimination of remaining carbon as carbon dioxide (from 420 to 550 °C, 2.1% mass loss). Pentan-2,4-dionato ligands therefore decompose in two successive steps according to two well-known processes: (i) a concerted reaction between two ligands and structural water,[30b,39] (ii) a retro-Claisen reaction catalyzed by the presence of Lewis acid such tin(IV) sites or water.[27,30b]

The texture of the xerogels prepared was also studied by transmission electron microscopy, thermoporometry, and N_2 sorption porosimetry to determine the effect of the hydrolysis ratio on the porosity and the surface areas. TEM photographs show that the as-prepared samples have a good porous structure, often called "worm-hole"- or "sponge"-like, with many small pores of 20−40 Å (Figure 2a). These features are consistent with thermoporometry calculations, with the dried samples showing average pore diameters ranging from 25 Å (G_{10}^{100}) to 35 Å (G_4^{100}).[36] Furthermore, BET surface areas and total pore volumes of about 330 m^2·g^{-1} and 0.39 cm^3·g^{-1} were measured for G_{10}^{100}; a decrease to 240 m^2·g^{-1} and 0.16 cm^3·g^{-1} was observed for the sample prepared with a lower hydrolysis ratio (G_4^{100}) (Table 1). In addition, it must be underlined that these morphological data remain unchanged after a one-year storage period in air. However, the shape of the N_2 adsorption isotherms indicates a more intricate texture. Thus, the N_2-adsorption measurements of G_{10}^{100} reveal a composite type I + type IV isotherm shape, typical of solids including both micro- and mesopores (Figure 3a). This was assessed by nitrogen *t*-plot analysis which led to a microporous surface and volume of about 35 m^2·g^{-1} and 0.008 cm^3·g^{-1}, respectively. XRD measurements are in

Table 1. Nitrogen Sorption Porosimetry Studies[a] of Dried and Calcined Sol−Gel Samples

sample	S_{BET} (m^2/g)	total pore volume (cm^3/g)	mean pore diameter (Å)
G_4^{100}	235	0.16	[b]
G_4^{400}	120	0.11	35
G_4^{450}	92	0.14	43
G_4^{500}	74	0.13	48
G_4^{550}	49	0.15	83
G_{10}	330	0.39	[b]
G_{10}^{400}	130	0.20	44
G_{10}^{450}	115	0.22	52
G_{10}^{500}	79	0.24	85
G_{10}^{550}	65	0.20	86

[a] Surface areas were determined by BET, mean pore diameters were determined by BJH theory (desorption branch), and pore volumes were obtained by single-point analysis. [b] BJH theory cannot be used to estimate the pore size in this case.

agreement with this complex porosity. Indeed, the low-angle X-ray diffraction pattern of the as-prepared samples shows no distinct peak which reveals a disordered porous structure and, in particular, a lack of long-range ordering in the mesostructure. The wide-angle XRD pattern of the xerogels shows very broad bands, the positions of which fit rather well with reported peaks for the tin dioxide cassiterite phase (Figure 4b).[40]

Characterization of the Annealed Xerogels. According to the TGA-MS results described above, xerogels were then treated in air at a temperature higher than 400 °C. The duration of the thermal treatment was fixed at 30 min in order to keep good textural properties and to reach very low amounts of remaining carbon.

Below 1600 cm^{-1}, the IR spectra of the calcined samples show four bands at ca. 667, 609, 540 (sh), and 470 cm^{-1} falling into the range of the Sn−O stretching mode region.[36] As a consequence, the intense band found at ca. 540 cm^{-1} (Sn−OH stretching mode) in the spectrum of the dried samples strongly decreased upon annealing and two new bands at 609 and 470 cm^{-1} appeared. The latter bands were assigned respectively to the antisymmetric and the symmetric Sn−O−Sn stretching mode of the surface-bridging oxide formed by condensation of adjacent surface hydroxyl groups with the concomitant release of water.[41] The relative intensities of these bands slightly varied when the temperature of the thermal treatment was increased up to 550 °C. These spectral changes can be easily related to changes in the shape and size of the SnO_2, as it was reported that for SnO_2 particles of different size and shape the antisymmetric and symmetric Sn−O−Sn IR bands can appear at different wavenumbers.[42] Consequently, these IR data account for the complete removal of the chelating ligands and the formation of more condensed particles.

As expected, calcination also strongly affects the structure, the texture, and the morphology of the samples, the same trend being observed for both hydrolysis ratios used. Thus, it was found that the XRD

(39) Di Maggio, R.; Campostrini, R.; Guella, G. *Chem. Mater.* **1998**, *10*, 3839.

(40) Powder diffraction file. JCPDS International Center for Diffraction Data: Swartmore, PA, 1997; no. 41-1445.

(41) (a) Harrison, P. G.; Guest, A. *J. Chem. Soc., Faraday Trans 1* **1987**, *83*, 3383. (b) Harrison, P. G.; Lloyd, N. C.; Daniell, W.; Bailey, C.; Azelee, W. *Chem. Mater.* **1999**, *11*, 896.

(42) Ocana, M.; Serna, C. J.; Matijevic, E. *Colloid. Polym. Sci.* **1995**, *273*, 681.

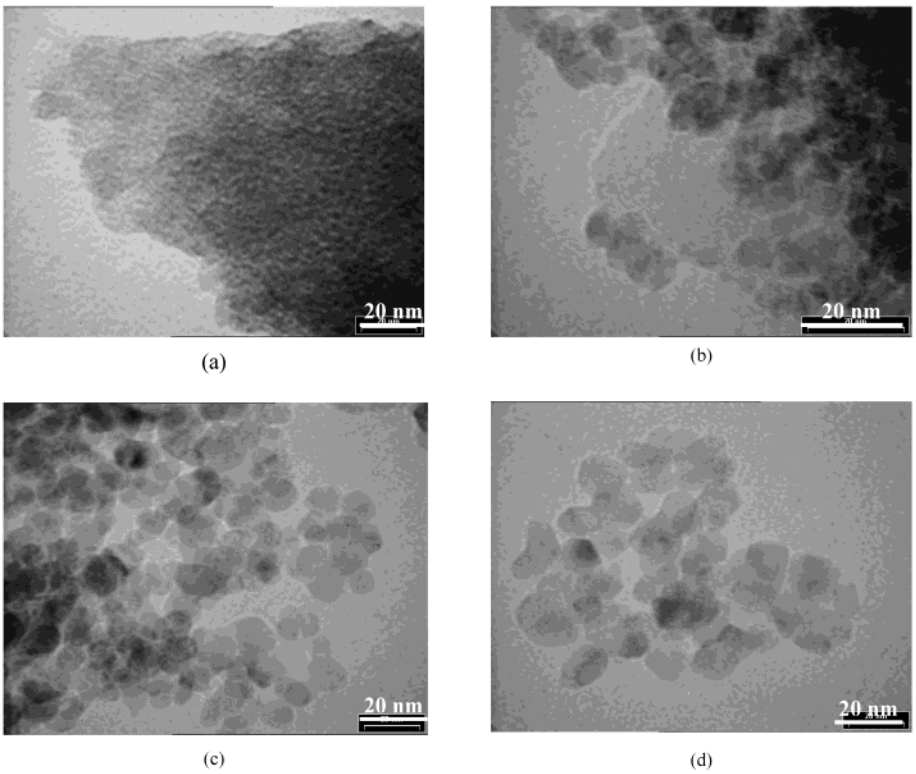

Figure 2. Transmission electron micrographs of (a) G_{10}^{100}, (b) G_{10}^{400}, (c) G_{10}^{450}, and (d) G_{10}^{550}.

Table 2. Values of the Mean Crystallite Size, Mean Particle Size, and Chemical Composition

sample	mean crystallite size[a] (Å)	mean particle size[b] (Å)	C/Sn (at. %)
G_4^{450}	40	70	5.5
G_4^{550}	70	160	2.5
G_{10}^{450}	36	80	6.5
G_{10}^{550}	77	180	4.0

[a] Determined from X-ray line broadening. [b] Determined from TEM photographs.

peaks of the calcined xerogels become progressively sharper with increasing the temperature of the thermal treatment, indicating the increase in crystal size due to sintering process (Figure 4c and d). The XRD patterns recorded for G_4^{550} and G_{10}^{550} clearly indicate the formation of SnO_2 cassiterite particles. Average nanocrystallite sizes of about 45 and 70 Å were estimated from the Debye-Scherer formula[43] for G_{10}^{450} and G_{10}^{550}, respectively (Table 2). TEM micrographs also reveal these drastic changes. After thermal treatment at 400 °C, the powder consists of aggregated nanoparticles of various sizes and shapes with some remaining amorphous areas (Figure 2b), but only nanoparticles were observed above 450 °C (Figure 2c and d). The mean particle size varied from 60−80 Å to 170−200 Å when the annealing temperature was progressively increased up to 550 °C. This phenomenon is concomitant with a strong decrease of the specific area. Indeed, the BET surface areas were found to be 115 and 65 $m^2 \cdot g^{-1}$ for G_{10}^{450} and G_{10}^{550}, respectively, with slightly lower values (95 and 50 $m^2 \cdot g^{-1}$) being measured for G_4^{450} and G_4^{550}. Nonetheless, the annealed samples still show a mesoporous structure. Indeed, the N_2 adsorption measurements of the calcined xerogels exhibit a pure type IV isotherm shape with a type H_2 hysteresis loop, typical of mesoporous solids prepared by the sol−gel route (Figure 3b and c).[44] In this case, the properties of the porous texture can be deduced from the BJH plot shown in Figure 3b and c. For instance, G_{10}^{450} has a fairly narrow pore size distribution, ca. 35−55 Å, with an average pore diameter of about 50 Å. This distribution is in rather good agreement with that inferred from thermoporometry measurements (Figure 5). For G_4^{550} and G_{10}^{550}, the pore size distributions are broadened and the average pore sizes increased up to 90−100 Å.

Discussion

This study shows that bis(2-methylbutan-2-oxy)di-(pentan-2,4-dionato)tin **1** is a suitable sol-gel precursor of mesoporous SnO_2 materials. Indeed, porous materials are classified by IUPAC on the basis of pore diameters as microporous (<2 nm), mesoporous (between 2 and 50 nm), and macroporous (> 50 nm).[45] Consequently, the porosity detected by N_2 adsorption measurements and thermoporometry in the case of both dried and calcined samples clearly falls into the mesoporous range.

The procedures described gave stable in time xerogels (at room temperature) with reproducible morphologies. Hydrolysis−condensation processes gave insoluble oxo-hydroxotin polymers containing at least 74% of SnO_2

(43) The mean particle size is given by the Laue-Scherrer relation $t = (\lambda/\epsilon \cos \theta)$, with $\epsilon = (\epsilon_m^2 - \epsilon_0^2)^{1/2}$ where θ is the Bragg angle for the chosen *hkl* reflection, ϵ_m and ϵ_0 are the angular half-widths of the *hkl* peak for the studied sample and well-crystallized SnO_2 without size effect, respectively. See Eberhardt, J. P. In *Structural and Chemical Analysis of Materials*, John-Wiley & Sons: New York 1991; p. 203.

(44) Rouquerol, F.; Rouquerol, J.; Sing, K. *Adsorption by Powders & Porous Solids*; Academic Press: London, 1999; p 204.

(45) Sing, K. S. W.; Everett, D. H.; Haul, R. A. W.; Moscou, L.; Pierotti, R. A.; Rouquerol, J.; Siemieniewska, T. *Pure Appl. Chem.* **1985**, *57*, 603.

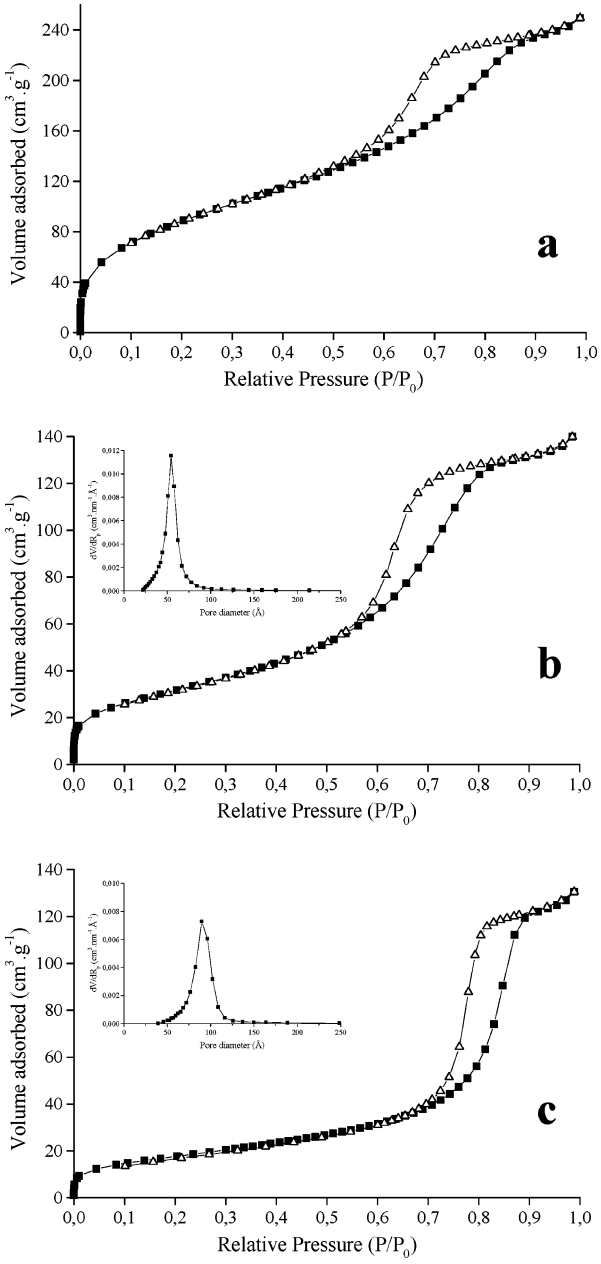

Figure 3. Nitrogen gas adsorption−desorption isotherms and BJH pore-size distribution (inset) of (a) G_{10}^{100}, (b) G_{10}^{450}, and (c) G_{10}^{550}.

and released to a large extent most of the pentan-2,4-dionato ligands. The higher hydrolysis ratio favored the formation of mesoporous xerogels with high surface areas and low mean pore diameters. Thus, after drying, the highest hydrolysis ratio, i.e., 10, yielded samples containing 83% of SnO_2 and exhibiting the largest BET specific area (330 $m^2 \cdot g^{-1}$) and the smallest pore size (25 Å). These results can be compared to those previously reported by Sanchez et al.[29] The surface areas and the SnO_2 amount obtained here are noticeably higher when samples prepared in acetonitrile are compared. It must, however, be noted that higher specific areas have been reported for samples synthesized in dioxane (350−410 $m^2 \cdot g^{-1}$), but merely comprising 61−64% of SnO_2.[29] The origin of the improvement described here is not yet clearly understood. However, it might stem from the drying step. Instead of a drying at 50 °C, the thermal treatment at 100 °C in a vacuum used in this study

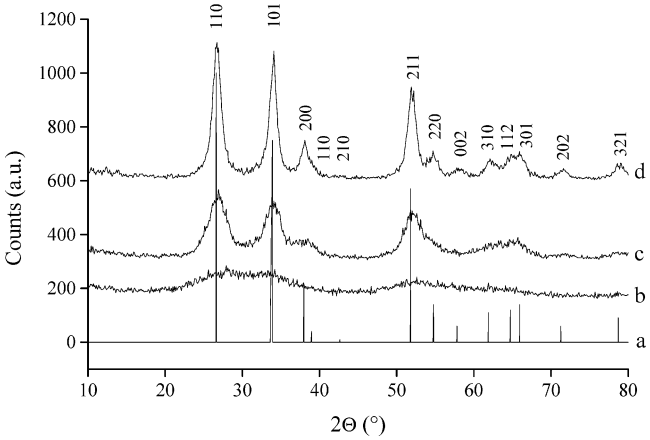

Figure 4. X-ray diffraction patterns of (a) cassiterite SnO_2 (JCPDS no. 41-1445), (b) G_{10}^{100}, (c) G_{10}^{450}. and (d) G_{10}^{550}.

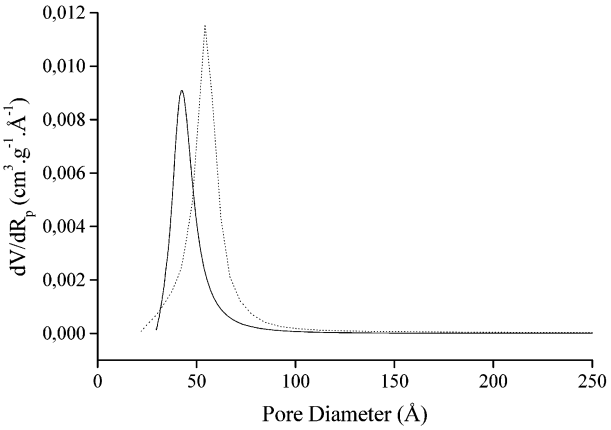

Figure 5. Differential distribution of pore volumes obtained for G_{10}^{450} using thermoporometry (full line) and BJH calculation (dotted line).

could have favored the release of the remaining organics and, as a consequence, the formation of additional pores. Furthermore, one has to emphasis that thermoporometry gave a better insight on the mesopore size distribution than the more popular BJH model. Thus, the samples mainly contain primary mesopores within the range 20−40 Å as revealed by TEM photographs. Thermoporometry calculations fit very well these values. In contrast, the assumptions of the BJH theory, which is based on the well-known Kelvin equation applied to the desorption branch of the N_2 adsorption isotherm, limit its scope to samples with pores larger than 34 Å in diameter, from which N_2 is desorbed at a pressure $p/p_0 = 0.42$.[46] This has therefore prevented the use of this model to estimate the pore size distribution of the xerogels.

As far as the calcined samples are concerned, the TEM and N_2 adsorption data can be rationalized as follows. Upon annealing, the low-temperature porous structure was spoiled and was replaced by a porous network of aggregated nanoparticles. The mesoporosity detected by N_2 adsorption measurements should therefore be attributed to the interparticle space. Furthermore, crystallization and sintering of the SnO_2 particles

(46) (a) Burgess, C. V. G.; Everett, D. H. *J. Colloid Interface Sci.* **1970**, *33*, 611. (b) Gregg, S. J.; Sing, K. S. W. *Adsorption, Surface Area and Porosity*, Academic Press: London, 1982; pp. 154−160. (c) Galarneau, A.; Desplantier, D.; Dutartre, R.; Di Renzo, F. *Microporous Mesoporous Mater.* **1999**, *27*, 297.

gradually occurred as the temperature of the thermal treatment was increased, likely via oxolation reactions:

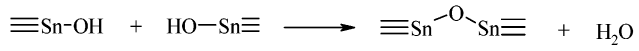

This process is fully consistent with the release of structural water at high temperature pointed out by TGA-MS. However, the particles sizes obtained from TEM photographs are larger than crystallite sizes deduced from X-ray diffractograms. This discrepancy may be explained by postulating the presence of structural defects (twins or macles) inside the nanoparticles which decreases the size of the monocrystalline domains and, as a consequence, broadens the XRD peaks.

If one considers the most favorable conditions for obtaining nanocrystalline mesoporous SnO_2 with high specific areas, i.e., $h = 10$ and thermal treatment at 450 °C, the BET surface area (115 $m^2 \cdot g^{-1}$) and the average pore size diameter (45−50 Å) are close to those reported for SnO_2 materials prepared by the organic surfactant route after treatment in the same temperature range.[3c,24,47] This specific area is comparable to those measured for siliceous composite after normalization for the difference in density between SiO_2 and SnO_2 (equivalent to 350 $m^2 \cdot g^{-1}$ for SiO_2). Furthermore, the carbon amount of the calcined samples is low. As a result, they could be used as active materials for various applications. In particular, G_4^{550} and G_{10}^{550} possess the textural properties to be good candidates as metal oxide materials in dye-sensitized solar cells. Indeed, Zaban et al. have recently shown that the use of 18-nm SnO_2 colloids exhibiting BET surface areas of about 60 $m^2 \cdot g^{-1}$ has permitted doubling of the light-to-energy conversion efficiency of the corresponding devices. Moreover, it is also worthwhile to mention that the calcined samples are stable after subsequent thermal treatment below 300 °C for several hours. Therefore, they might be advantageously used to detect nitrogen monoxide since, in this case, the working sensor temperature is about 200 °C.[48]

Conclusion

Nanocrystalline mesoporous tin dioxide materials have been prepared through the controlled hydrolysis of bis(2-methylbutan-2-oxy)di(pentan-2,4-dionato)tin followed by a thermal treatment at 400−550 °C. The materials consist of a porous network of aggregated nanoparticles; the mesoporosity observed corresponding to the interparticle space. A careful tuning of both hydrolysis ratio and calcination temperature enabled us to prepare powders with surface areas ranging from 50 to 150 $m^2 \cdot g^{-1}$, with an average pore size between 45 and 100 Å and with a mean particle size ranging from 60 to 180 Å. In addition, the use of high hydrolysis ratios constitutes the best strategy to get the larger surface area and the lower mean pore size diameter. Using these powders as semiconducting metal oxide materials, we are undertaking the development of dye-sensitized photoelectrochemical cells.

Acknowledgment. Prof. F. Rouquerol is acknowledged for helpful discussion. Dr. G. Campet is thanked for the XRD measurements and Mrs. Rascle is thanked for her precious assistance. This work was supported by the Centre National de la Recherche Scientifique, the MENRT (G.V. fellowship and ACI Jeunes Chercheurs grant) and the Aquitaine Region.

Supporting Information Available: Figures of IR spectra, thermogravimetrical (under air), DSC analyses, and TGA-MS ion fragment trends of the dried or calcined xerogels. This material is available free of charge via the Internet at http://pubs.acs.org.

CM0344459

(47) Li, G. J.; Kawi, S. *Mater. Lett.* **1998**, *34*, 99.

(48) Zhang, G.; Liu, M. *Sens. Actuators, B* **2000**, *69*, 144.